Interface interaction mediated surface plasmon resonance enhancement promoted visible-light-driven CO_2 reduction with water

Huiming Wang [a], Sheng Xu [a], Baoxin Ni [a], Jinting Xu [a], Gregory A. Solan [c], Shuaiqi Gong [a,*], Yulin Min [a,b,**]

[a] *Shanghai Key Laboratory of Materials Protection and Advanced Materials in Electric Power, Shanghai University of Electric Power, Shanghai 200090, China*
[b] *Shanghai Institute of Pollution Control and Ecological Security, Shanghai 200092, China*
[c] *Department of Chemistry, University of Leicester, University Road, Leicester LE1 7RH, UK*

A R T I C L E   I N F O

A B S T R A C T

The conversion of carbon dioxide (CO_2) into fuel using solar energy holds significant promise. However, the inefficient use of light and poor production activity have hindered its development. Here, we propose a simple *in situ* annealing oxidation method by coating a layer of TiO_2 outside TiN, a material with a favorable price and localized surface plasmon resonance (LSPR) effect, to create an L-TiNO composite. The yield of CO over L-TiNO (50.8 µmol g^{-1} h^{-1}) is 56.4 times that over TiO_2 (0.9 µmol g^{-1} h^{-1}) under visible light irradiation in pure aqueous environment, with a selectivity of 95.98%. *In-situ* Fourier transform infrared (FTIR) measurements reflect the CO_2-COOH*-CO conversion route happening on L-TiNO. Characterizations like the Kelvin probe force microscopy (KPFM) technique confirm the generation of built-in electric field, which facilitates efficient carrier separation and migration. Density functional theory (DFT) calculations support that L-TiNO with LSPR effect alters the shape of absorbed CO_2 to facilitate generation COOH* via forming hydroxyl end group (Ti-OH) and promotes CO* desorption to CO(g). This work provides valuable insights into the coupling of plasmonic materials with semiconductors to achieve efficient solar energy utilization.

1. Introduction

The utilization of abundant solar energy to convert carbon dioxide (CO_2) and water into value-added chemicals and fuels is tipped to mitigate the dangers posed by the greenhouse effect and to address energy shortages by converting light energy into chemical energy for storage [1]. Extensive researches were dedicated to exploring materials suitable for light-driven CO_2 reduction, considering factors such as the type of products generated (C_1 or C_{2+}), reaction efficiency and product selectivity [2–6]. Normally, photocatalytic materials have primarily centered on semiconductors, such as the traditional photocatalyst titanium dioxide (TiO_2) [7]. However, the reduction of CO_2 on semiconductors always faces the issue of poor conversion rate, which is mainly caused by the lack of efficient photogenerated carriers [8,9]. Furthermore, the adsorption and activation of CO_2 on the surface of photocatalysts are key factors to determine the reaction rate. Thus, the fragmentation of CO_2 adsorption sites and photogenerated electron aggregation sites hinders the kinetics of the reaction [10].

Plasmonic nanomaterials owning unique localized surface plasmon resonance (LSPR) effects have shown great potential in improving photocatalytic efficiency [11]. The collective oscillation of free charge carriers in plasmonic materials, called as LSRP effect, would not only broaden the light response range, but also induce a greatly enhanced localized electric field to facilitate charge transfer on the surface of the photocatalyst. This strong surface-localized electric field can convert photon energy into surface plasma excitons, thereby driving the photocatalytic reaction and improving the reaction rate [12–15]. On top of that and more interestingly, the excited-state electrons in localized surface plasmons can generate high-energy hot electrons and hot holes through non-radiative decay, providing additional hot electrons for the reaction [16]. These extra hot electrons can synergistically interact with the photogenerated electrons, aiding in lowering the reaction barrier and achieving kinetically challenging multi-electron reactions. This effectively addresses the difficulty of a scarcity of effective charge

carriers in photocatalytic reduction reactions, thereby enhancing the efficiency of the reaction. Currently, research on plasma catalysts primarily focuses on the utilization of metal nanoparticles especially noble metals[17], such as silver[18], gold[19], and copper[20], which greatly limits the large-scale application. In this regard, it is crucial to search for non-noble metal materials with LSPR effects. Titanium nitride (TiN) is a compound composed of titanium and nitrogen, with a metal gap structure. It exhibits LSPR absorption peaks over a wide wavelength range, which means that when illuminated by light, TiN can absorb specific wavelengths of light, giving it the ability to excite surface enhanced spectra [21–24]. Therefore, TiN has great potential as a candidate to replace noble metal plasmonic materials [25,26]. However, the application of pure plasmonic materials as photocatalysts is hindered by the extremely short lifetime of hot carriers (typically 10–100 ps), which is incompatible with the slow timescale of chemical reactions (several milliseconds or seconds) [27].

The integration of LSPR materials and semiconductors is an effective approach to address the aforementioned issues. The contact between LSPR materials and semiconductors enhances light absorption by the semiconductors[28]. Additionally, the interface between these materials generates an electromagnetic field that induces carrier motion within the semiconductor, leading to the formation of a Schottky barrier that effectively limits electron movement. Consequently, this enables control and modulation of electron behavior and leads to improved efficiency in photocatalytic reactions. TiO_2, a reducible metal oxide widely used in CO_2 photoreduction, can be grown as a thin layer on the surface of TiN nanoparticles. This construction can achieve the formation of Schottky barriers and strong surface oxide–support interaction (SOSI). It can not only benefit from the LSPR effect to promote charge carriers, but also increase the active sites on the surface and change the electronic structure of the carrier to improve photocatalytic activity and stability through SOSI [29]. On top of that, the SOSI also plays a promoting role in the hydrogen spillover effect, which refers to the phenomenon where hydrogen atoms dissociate on the active site surface and migrate to the support [30]. Upon the formation of the metal oxide-support interface, atomic H species can migrate along the reducible metal oxide (such as TiO_2) surface through coherent proton-electron motion, with the interface serving as a pathway for H species transport [31]. As a result of hydrogen spillover, CO* on the active sites cannot undergo further hydrogenation but directly desorb as CO, leading to the reverse water-gas shift (RWGS) reaction and enhancing the selectivity of CO_2 reduction to CO [32].

As mentioned above, the design of photocatalytic materials such as TiO_2@TiN with Schottky barrier and SOSI can effectively harness the LSPR effect to enhance photocatalytic activity and improve CO selectivity through hydrogen spillover, so that shows great potential for achieving high efficiency and selectivity in CO_2 photoreduction to CO. Herein, 500 nm TiN nanoparticle supports were partially oxidized by annealing to *in-situ* construct TiO_2 oxide layers, resulting in interfacial smooth thin layer-coated TiO_2@TiN composites (L-TiNO). Theoretical calculations and experiments, including the photo-assisted Kelvin probe force microscopy (KPFM) technique, have confirmed the LSPR effect of hot electrons and a strong local electric field on L-TiNO. These investigations have also demonstrated the effective LSPR effect would regulate the electronic structure, promote the generation and efficient utilization of charge carriers, and enhance CO_2 adsorption, all of which are crucial for improving CO_2 photoreduction activity. *In-situ* Fourier transform infrared (FTIR) spectra provided insights into the evolution of COOH* (a key intermediate during CO_2 reduction) and CO* adsorption, indicating the effect of hydrogen spillover on CO_2 reduction to CO, which was facilitated by the SOSI effect between TiO_2 and TiN support. L-TiNO exhibited remarkable catalytic activity for CO_2-to-CO conversion with a rate of 50.8 μmol g^{-1} h^{-1} and a selectivity of 95.98% in pure water under visible light irradiation. This work opens new avenues for designing advanced RWGS catalysts.

2. Experimental section

2.1. Synthesis of L-TiNO

L-TiNO samples were prepared using a simple strategy of slow thermal oxidation of TiN starting particles. TiN nanoparticles were purchased from Admas with an average particle size of 500 nm. The TiN samples were first taken about 30 mg in a boat-shaped ceramic perimeter and then placed in a muffle furnace at an elevated temperature rate of 1 °C/min to the corresponding temperatures (400–800 °C) and kept at these temperatures for 1 h. The L-TiNO samples were prepared by cooling the annealed samples naturally to room temperature.

2.2. Photocatalytic CO_2 reduction tests

Three-phase photocatalytic CO_2 reduction tests were carried out in a closed quartz reactor with gas circulation. In order to prepare for the tests, a quantity of catalysts was evenly distributed in 100 mL of deionized water, resulting in a catalyst concentration of 0.4 g/L. Afterward, the mixture underwent sonication for a duration of 1 h. Subsequently, the reactor was subjected to evacuation, followed by purging with pure argon gas for a period of 20 min. This process aimed to eliminate any residual air that might have been present. Subsequently, the reactor was filled with CO_2 (99.999%) at a pressure of 1.01 bar. The light irradiation experiments were conducted using the PLS-SXE300D xenon lamp from PerfectLight. To control the wavelength of the light, a cut-off filter was employed. The analysis of the reduction products was performed using an on-line gas chromatograph (GC-2014, Shimadzu) that was equipped with a thermal conductivity detector (TCD) and two flame-ionization detectors (FIDs). Argon (Ar) was utilized as the carrier gas for the analysis. The instrument employed the SH-Rtx-Wax column model, which had a film thickness of 0.25 μm, an inner diameter (ID) of 0.25 mm, and a length of 30 m.

2.3. Measurement of SERS performance

In the standard procedure, 1 mg of the powder sample was homogeneously dispersed in 1 mL of a 10^{-5} M aqueous solution of Methylene Blue (MB) using ultrasonication for a duration of 10 min. Following the settling period of 20 min to aid in the separation of solid particles, the mixture underwent centrifugation. The resulting precipitate was then carefully transferred onto a pristine silicon (Si) wafer. The sample on the wafer was then dried at room temperature. For the blank sample, a 50 μL droplet of the desired solution (without the powder sample) was directly dropped onto a clean Si wafer and dried at room temperature. Raman spectra were collected using a confocal Raman/PL (Photoluminescence) system, specifically the LabRamHR Evolution. The system was equipped with a 532-nm laser source, which emits light at a wavelength of 532 nanometers. The Raman spectra were obtained by measuring the scattering of the laser light from the samples on the Si wafer.

2.4. KPFM measurements

Kelvin Probe Force microscopy measurements (KPFM) were conducted using SHIMADZU SPM-9700HT. The light source was a Mercury lamp with a wavelength of 180 ~ 500 nm to avoid the effect the AFM signal. The sample was dispersed on FTO. During the testing, the sample was irradiated by the light source with quartz optical fiber. The lift mode was utilized with a lift height ranging from 50 to 100 nm during surface potential measurements.

3. Results and discussion

3.1. Synthesis, structural characterization and optical properties of L-TiNO

To address the issue of short hot carrier lifetimes in plasmonic materials that limits their direct application, we developed a method to grow TiO_2 semiconductor *in-situ* on the surface of TiN. By leveraging the strong oxide-support interaction at the interface, we facilitate the transfer of hot electrons from the plasmonic material TiN to the semiconductor TiO_2, thereby extending the lifetimes of the carriers and creating a composite photocatalyst (L-TiNO) with highly covered active sites for carriers. Fig. 1a shows the overall synthesis process with annealing in air directly and the detailed method is described in the experimental section in Supplementary information. The average particle size of the chosen commercial TiN is 500 nm. The range of annealing temperature is controlled between 400 and 800 ℃. The thickness of the oxide layer on the TiN surface, which plays a crucial role in transferring hot carriers from the plasmonic TiN to the TiO_2 activate site, is controlled by the calcination temperature. The dominant sample discussed in this paper (which is named L-TiNO) is calcinated at 500 ℃ for 1 h. The relationship between oxidation temperature and oxidation degree is examined by the thermogravimetric analysis (TGA) of TiN. As shown in Figure S1, the oxidized weight gain of TiN started at 487.39 ℃ and reached its endpoint at 753.9 ℃. This guides our design that calcinating at 500 ℃ to obtain the desired TiO_2 thin layer coating on TiN and at 800 ℃ TiN can be transferred to TiO_2 completely.

Scanning electron microscopy (SEM) images (Figure S2) show that no apparent morphological differences can be observed between TiN, L-TiNO, and TiO_2, indicating that the formation of TiO_2 in the L-TiNO composite originates from the replacement of nitrogen (N) atoms in TiN by oxygen (O) atoms. Focusing on the more detailed transmission electron microscopy (TEM), it can be found that L-TiNO exhibits core-shell structure (Fig. 1b), in comparison to the solid nanoparticle of commercial TiN (Figure S3). The high-resolution TEM (HRTEM) image of L-TiNO, as presented in Fig. 1c, reveals a distinct grain boundary between TiO_2 and TiN. The core portion displays a lattice distance of 0.2398 nm corresponding to the (111) crystallographic plane of TiN, and the out layer (shell part) shows the lattice fringe of 0.3297 nm corresponding to the (110) crystallographic plane of rutile phase TiO_2. It is worth noting that the small lattice spacing change observed is attributed to the stress balance between the introduction of lattice O and the precipitation of lattice N, since the ionic radius of N^{3-} (0.171 nm) is larger than that of O^{2-} (0.132 nm). The core-shell structure confirms the O replacing process that occurs from the outer edge to the center of the nanoparticle during the *in-situ* fabrication of TiO_2 along TiN. Moreover, the line scan energy dispersion X-ray spectroscopy (EDX) image of L-TiNO, as depicted in Fig. 1d, displays that the elemental O content is higher on both sides of the sample, while the N content is predominant in the central part of the sample. EDX elemental mapping (Fig. 1e) provides further evidence for the localization of N elements in the central core of the hybrid material. These observations suggest that TiN is oxidized into TiO_2 from the outside to the inside, resulting in the formation of a composite with a thin TiO_2 layer coating on TiN. The HRTEM images of pure TiN and TiO_2 are presented in Figure S4. The insets in the upper right corner of Figures S4a and S4b refer to the lattice enlargements of TiN and TiO_2. The measure of partially oxidizing TiN to build TiO_2 can disrupt the solid morphology of TiN nanoparticles,
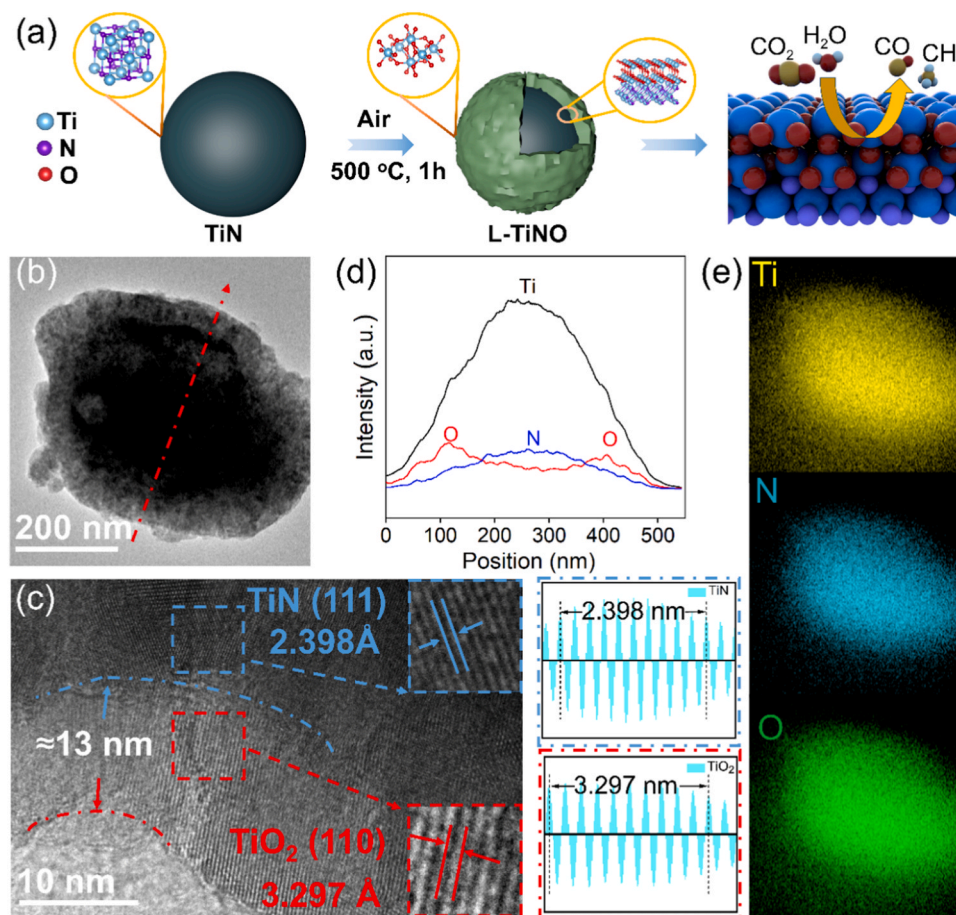

Fig. 1. (a) Synthetic procedure of L-TiNO. (b) TEM image and (c) HRTEM image of L-TiNO. (d) Corresponding elemental line scans and (e) EDX elemental mapping images of (c).

increase the specific surface area, and thus expose more active sites, which is beneficial for promoting catalytic reactions. As shown in N_2 adsorption/desorption isotherms in Figure S5, the oxidized L-TiNO sample has a higher specific surface area of 20.50 m^2/g than pristine TiN (14.83 m^2/g) and fully oxidized TiO_2 sample (14.62 m^2/g), suggesting the availability of active sites for carrying out carbon dioxide reduction.

X-ray diffraction (XRD) patterns were obtained and analyzed to further confirm the structure of the oxidized TiN, also known as L-TiNO. Pure TiN has the characteristic XRD pattern of a cubic F3M crystal structure (PDF # 38–1420, Fig. 2a and S6). After oxidization treatment, new peaks which are index to rutile phase TiO_2 (PDF # 21–1276) appeared, consistent with the formation of TiO_2/TiN heterostructure in L-TiNO (Fig. 2a). With prolonged annealing time and temperature, TiN crystal is completely converted into TiO_2, leading to the disappearance of TiN peaks with only rutile TiO_2 peaks leaving. The crystal structures of TiN, L-TiNO and TiO_2 are displayed in Fig. 2b.

The survey X-ray photoelectron spectroscopy (XPS) reveals the elemental distribution of the samples with varying oxidation degrees in Figure S7, supporting the idea that the oxidation treatment leads to an increase in O content and a decrease in N content, further confirming the transformation of TiN into TiO_2 in L-TiNO. And the occupied ratio of N and O contents in L-TiNO is about 17:7 according to Table S1, showing that the content of TiN L-TiNO occupies about 72%. In detail, N 1 s XPS high-resolution spectra of TiN and L-TiNO in Fig. 2c show distinct four peaks corresponding to different nitrogen chemical bonds. In TiN, the characteristic peaks at 396.03 eV and 401.05 eV are attributed to lattice

N (N-Ti bonds) and partial N (N-O bonds), respectively [33]. An oxidized component of the N-Ti-O bond at 397.13 eV and adsorbed ambient carbon-containing species (N-C bond, at 398.84 eV) can be explained by the exposed oxidization in air [34]. When TiN is surface oxidized to form L-TiNO, the peak of N-Ti-O bond with smaller area shifts toward the lower binding energy (396.64 eV) and the peak of N-O bond with bigger area shifts toward higher binding energy (401.62 eV) compared to their positions in TiN, indicating that O occupies N sites to coordinate with Ti sites and form TiO_2/TiN heterostructure with O-Ti-N interface. In the O 1 s region of TiO_2 (Fig. 2d), two peaks at 529.87 eV and 531.59 eV are attributed to the metal-oxygen bond (Ti-O) and oxygen defects, respectively [35]. However, in L-TiNO, the characteristic peaks of both Ti-O and oxygen defects shift to the direction of high binding energies (529.96 eV and 531.87 eV, respectively), indicating an electron-deficient state of the O atoms in L-TiNO. Moreover, the shifting features observed in the N 1 s and O 1 s spectra of L-TiNO suggest that the configuration of O-Ti-N interface may act as a bridge for the transfer of electrons from TiN to TiO_2, which implies the SOSI effect and the formation of built-in electric field from TiO_2 to TiN (this item will be discussed in a later section). Fig. 2e shows Ti 2p XPS spectra, which can be fitted into two spin-orbits doublets of Ti $2p_{3/2}$ and Ti $2p_{1/2}$. The chemical states of Ti in pure TiN are existed as Ti^{2+} (454.9 and 460.8 eV), Ti^{3+} (456.7 and 463.2 eV) and Ti^{4+} (458.4 and 464.3 eV) [36]. In comparison, the valence states of Ti in L-TiNO is only +4 without +2 and +3, further indicating oxidization occurs on TiN. In addition, the Ti^{4+} peak at 464.2 eV in L-TiNO shifts oppositely related to
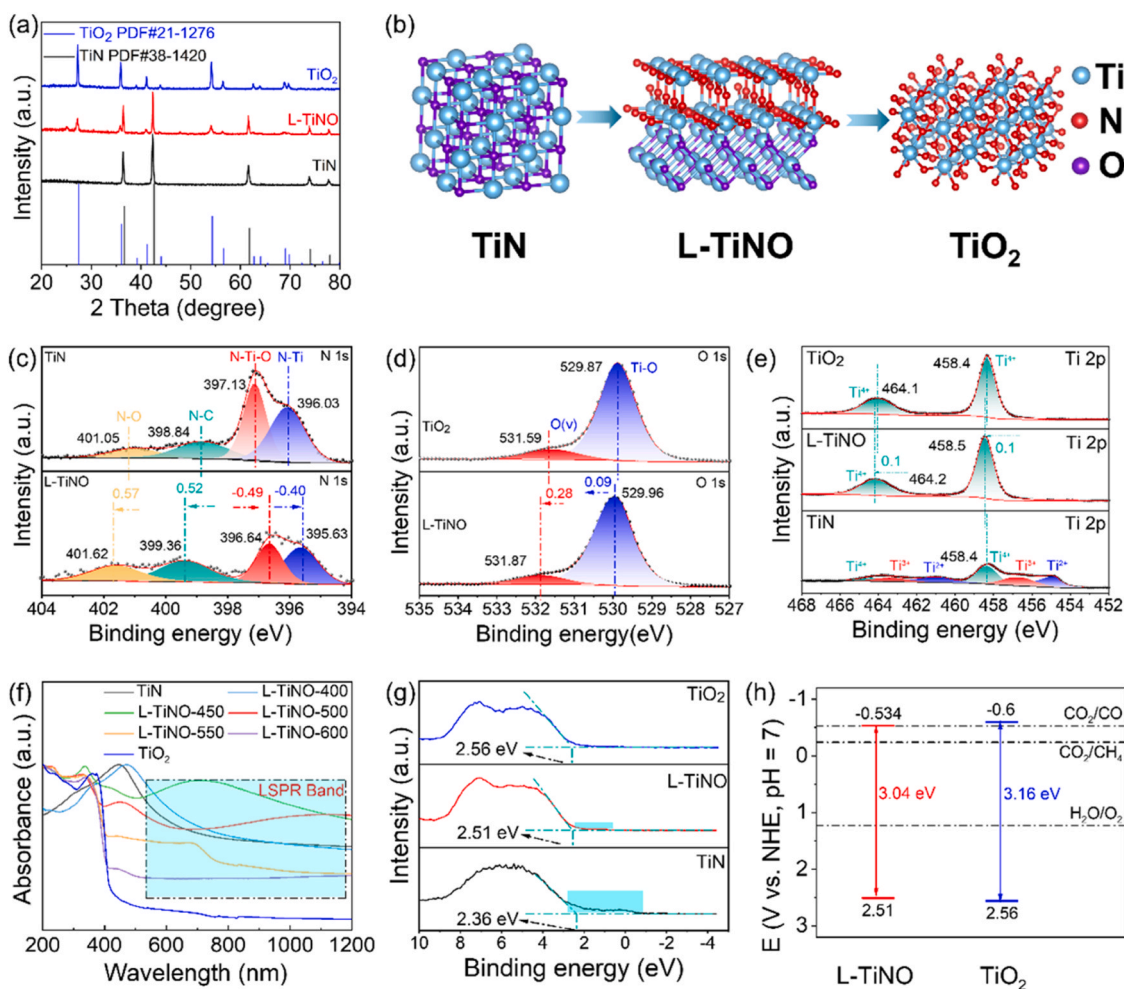

Fig. 2. (a) XRD patterns and (b) the corresponding crystal structures of TiN, L-TiNO and TiO_2. (c) N 1 s XPS spectra of TiN and L-TiNO. (d) O 1 s XPS spectra of L-TiNO and TiO_2. (e) Ti 2p XPS spectra of TiN, L-TiNO and TiO_2. (f) UV–vis DRS of TiN, L-TiNO-x (x = 400, 450, 500, 550, and 600) and TiO_2. (g) XPS-VB spectra of TiN, L-TiNO and TiO_2. (h) Band structures of TiO_2 and L-TiNO.

pure TiN (458.4 eV) and pure TiO_2 (464.1 eV), further indicating the electrons transfer from TiN to TiO_2 in L-TiNO.

The optical properties of photocatalysts, particularly their light absorption and suitable band edges, are crucial for their photocatalytic performance. Fig. 2f displays the UV–visible diffuse reflectance spectroscopy (UV–vis DRS) of the samples, revealing that TiN has a plasma resonance absorption peak in a wide region of 200 ~ 800 nm. This can be due to the LSPR effect, which arises from the oscillations of free electrons. The partially oxidized series of L-TiNO samples demonstrate optical absorption across a wide range of the solar spectrum, spanning from 200 nm to 1200 nm, including the intrinsic absorption edge of TiO_2 at around 380 nm and a broad absorption extending into near-infrared region which can be attributed to the plasmonic TiN. In detail, the plasma resonance absorption peak for series of L-TiNO samples show a slight red shift compared to the original TiN. This shift can be attributed to the difference in dielectric properties between TiN and TiO_2. More specifically, with the formation of TiO_2 (metal oxide semiconductor material with a high dielectric constant: 80–170) outside TiN (metal-ceramic material with a low dielectric constant: 5–10), the L-TiNO series samples are exposed to an environment with a high dielectric constant. In this scenario, the electrons are strongly shielded, leading to a reduction in the energy required for electron jumps and causing a red-shift in the absorption spectra. Additionally, the increase in annealing temperature and oxidation thickness leads to a decline in LSPR-induced optical absorption, indicating the hindering effect of a thick oxidation layer on LSPR transfer which effects the light absorption and catalytic reaction. After the TiN component is completely transferred to TiO_2, the UV–vis DRS analysis shows that only UV absorption is observed without the wide absorption caused by LSPR effect, indicating the lack of LSPR effect of pure TiO_2.

As shown in Tauc plots and Mott-Schottky plots (Figures S8), the energy gap (E_g) and conduction band (CB) of L-TiNO can be determined to 3.0 and −0.534 V (vs. NHE), respectively. According to the valence band (VB) spectra of XPS results (Fig. 2g), the apparent optical VB potentials are measured to be 2.36 eV for TiN, 2.51 eV for L-TiNO and 2.58 eV for TiO_2, respectively. Additionally, an obvious defect-band level appears near the Fermi energy level, which is induced by the localized electrons. The corresponding CB values of L-TiNO and TiO_2 are calculated to be −0.49 and −0.54 eV, respectively, well matched with the Mott-Schottky results. Based on these, the band structure of L-TiNO can be outlined in Fig. 2h. As a result, L-TiNO has suitable band edge positions to drive simultaneous CO_2 reduction to CO under visible light irradiation.

3.2. Photocatalytic activity of CO_2 reduction

Initial control tests conducted in Fig. 3a were designed to demonstrate the essential roles of light, catalyst, and CO_2 in the experimental setup. These control tests also confirm that the observed products are indeed originated from CO_2 instead of other carbon species. The compared performances of photocatalytic CO_2 reduction on the samples of varying TiN oxidation degrees were evaluated and the tests were carried out under visible light irradiation ($\lambda > 420$ nm) without any sacrificial agent in pure water. The reduction products are CO and CH_4. And there's no any liquid product according to the ^1H NMR result (Figure S9). Figs. 3b and 3c demonstrates that pure TiN has poor CO_2 photoreduction activity, resulting in low production rates of CO (11.09 µmol g^{-1} h^{-1}) and CH_4 (0.79 µmol g^{-1} h^{-1}), which may be attributed to the short lifetime of carriers for LSPR materials. When TiN is partially oxidized to TiO_2, there is a significant improvement in the photocatalytic CO_2 reduction performance. The production rates of CO and CH_4 increase due to the formation of TiO_2/TiN heterostructure. The performance tests of physically mixed samples of TiN and TiO_2 were carried out in Figure S10, which showed greatly decrease compared with L-TiNO, indicating the importance of the design of heterojunctions of TiN and TiO_2 core-shell structures in the photocatalytic reaction. Interestingly, as the oxidation of TiN increases and approaches a peak activity, the performances of CO and CH_4 evolution start to decease. This suggests that the thickness of the oxide layer plays a crucial role in transferring carriers. The sample labeled as L-TiNO-500, which is prepared at 500 °C for 1 h with a thin oxide layer, exhibits the highest CO and CH_4 evolution rates. This sample achieves a CO yield of 50.8 µmol g^{-1} h^{-1} and a CH_4 yield of 2.13 µmol g^{-1} h^{-1}, indicating its superior photocatalytic performance for CO_2 reduction. On top of that, L-TiNO-500 shows an excellently increased CO selectivity of 95.98%, which is greatly superior to pure TiN and TiO_2 in terms of both activity and selectivity. The lower activities of other samples with annealing temperature increase are mainly caused by the increase in thickness of the
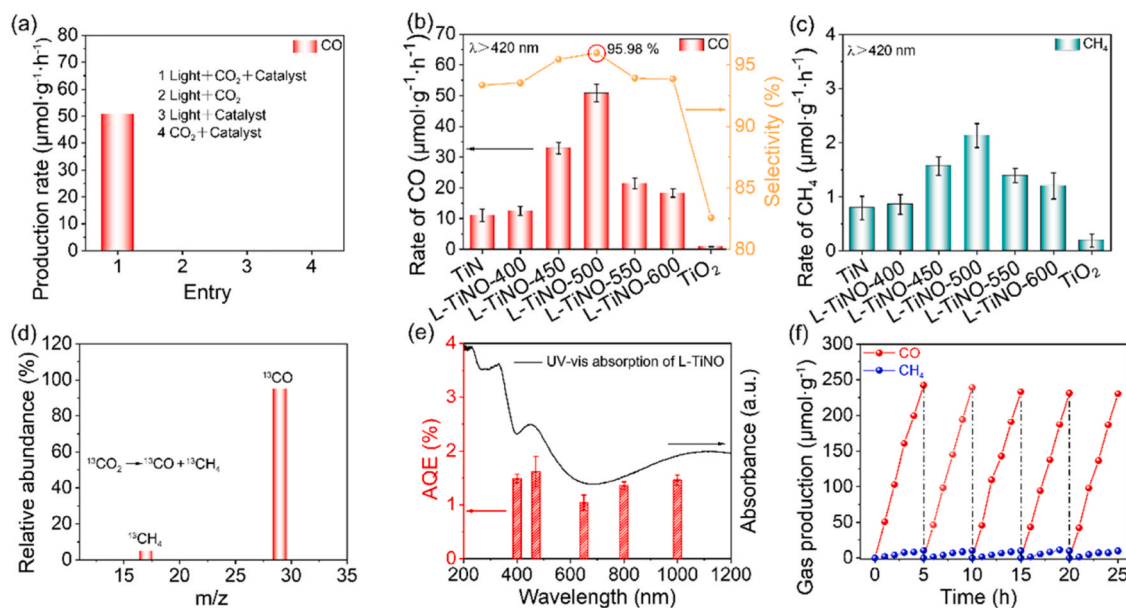

Fig. 3. (a) Initial control experiments. (b) CO yield rates and selectivity over TiN, L-TiNO-x (x = 400, 450, 500, 550, and 600) and TiO_2. (c) CH_4 yield rates over TiN, L-TiNO-x (x = 400, 450, 500, 550, and 600) and TiO_2. (d) Mass spectrum of the products after the $^{13}CO_2$ photocatalytic reduction over L-TiNO. (e) AQEs of L-TiNO. (f) Cycling test for photocatalytic CO_2 reduction over L-TiNO.

TiO$_2$ layer, which would extend the migrating path length of hot electrons to the catalyst surface, leading to increased electron-phonon scattering in the catalyst and reduced overall catalytic efficiency. In addition, as the thickness of TiO$_2$ oxide layer increases, the content of TiN in the composite decreases, indicating a reduction in the number of plasmas. This leads to a decrease in the photocatalytic activity for CO$_2$ reduction. The photocatalytic CO$_2$ reduction performance of L-TiNO occurred in pure water without sacrificial agent is competitive to those Ti-based photocatalysts (Table S2). Meanwhile, with the reduction of CO$_2$ to CO and CH$_4$, water is oxidized to O$_2$ (Figure S11).

Besides the control experiments in Fig. 3a, the ^{13}CO$_2$ labeling gas chromatography-mass spectrometry (GC-MS) experiment was then conducted to directly trace the carbon source of the products. As shown in Fig. 3d, distinct signals of ^{13}CO ($m/z = 29$) and ^{13}CH$_4$ ($m/z = 17$) are observed in the ^{13}CO$_2$ labeling GC-MS experiment, confirming the CO and CH$_4$ products are indeed originated from CO$_2$ instead other carbon species. The apparent quantum efficiencies (AQEs) for CO evolution over L-TiNO are calculated to be 1.62% under the monochromatic light illumination at a long wavelength of 450 nm indicating the efficient utilization of incident light (Fig. 3e). Meanwhile, the trend of the determined AQEs aligning well with the light absorption spectrum of L-TiNO suggests that the material's light absorption properties are well-matched to the wavelength of light used for the experiment (Fig. 3e and S12). This indicates that L-TiNO is able to efficiently absorb and utilize the specific wavelength of light for the catalytic reaction involving the enhanced light absorption caused by the LSPR effect. The stability test was performed under the same conditions over 5 cycles during a total reaction time of 25 h. As depicted in Fig. 3f, the decline on the production yields of CO and CH$_4$ is hardly observed, evidencing the reusability and robustness of the photocatalysts. Meanwhile, the XRD pattern and SEM image of L-TiNO after 25 h photocatalytic CO$_2$ reduction maintain the same characteristic peaks and morphology as the fresh samples, also confirming the high stability of the catalyst (Figure S13).

The LSPR effect can generate localized heating due to the absorption of light by plasmonic nanoparticles. To investigate the influence of the photothermal effect on photocatalytic CO$_2$ reduction, thermo-catalytic CO$_2$ reduction experiments were performed. The plasma heterojunction photocatalyst system (L-TiNO) was subjected to light irradiation, and the temperature rise resulting from the photothermal effect was monitored. Based on the results shown in Figure S14, it is evident that the photothermal effect, resulting from the localized heating caused by LSPR effect, does not promote photocatalytic CO$_2$ reduction in the L-TiNO system. This finding further indicates that the driven energy for CO$_2$ reduction primarily comes from light, and the active sites responsible for the catalytic reaction are mainly located on the TiO$_2$ component. The role of the LSPR TiN material is to provide additional hot electrons and generate alternative electric fields, aiming to enhance the CO$_2$ reduction activities.

3.3. Mechanism on plasmon-induced catalytic process and charge-carrier dynamics

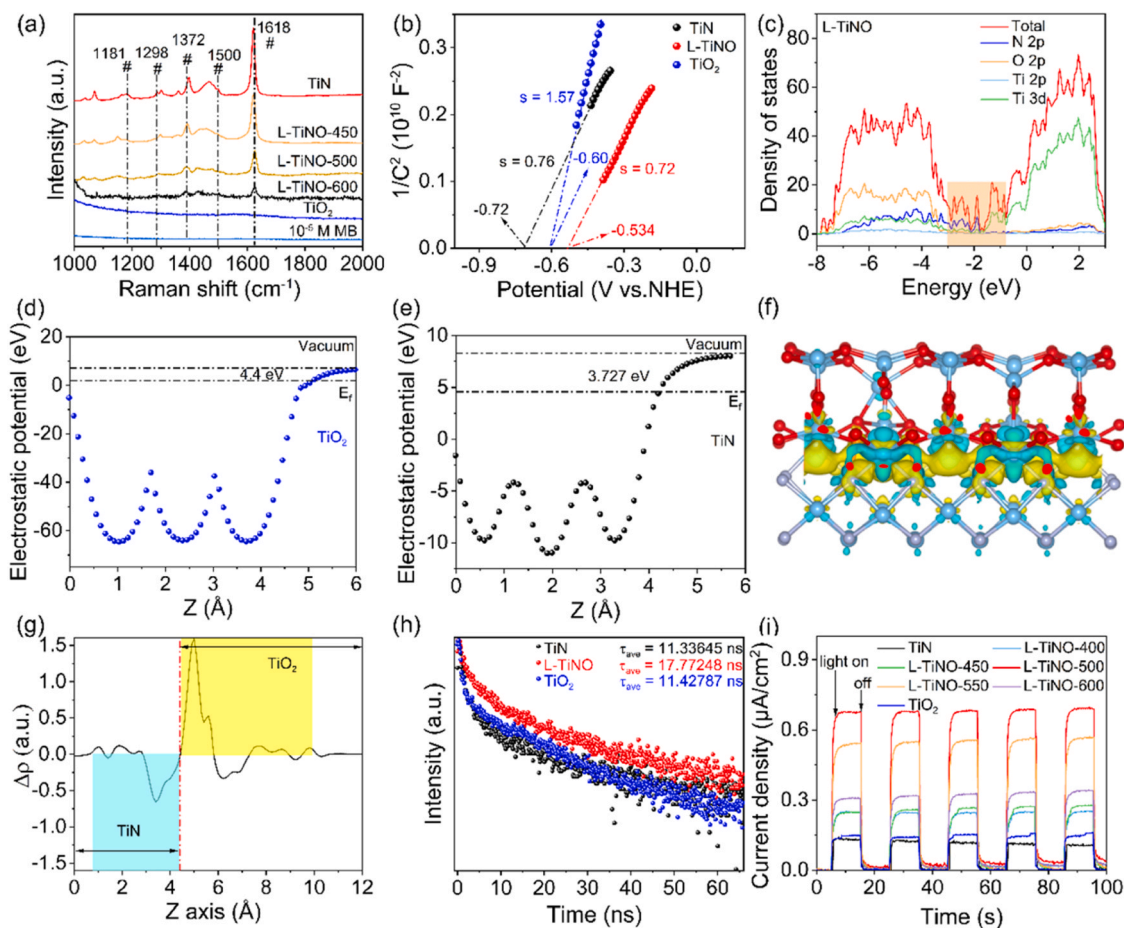To investigate the reasons behind the performance improvement, we

Fig. 4. (a) Raman spectra of MB (1.0×10^{-5} M) collected on TiN, L-TiNO-x (x = 400, 450, 500, 550, and 600) and TiO$_2$. (b) Mott-Schottky plots of TiN, L-TiNO and TiO$_2$. (c) PDOS of simulated L-TiNO. Electrostatic potentials of (d) TiO$_2$ and (e) TiN (Vacuum: vacuum level; E$_F$: Fermi level). (f) Charge density differences of L-TiNO (yellow: electron aggregation; blue: electron depletion). (g) Profile of the planar averaged charge density difference Δρ (z) for L-TiNO. (h) TRPL spectra and (i) photocurrent response of TiN, L-TiNO and TiO$_2$.

conducted researches on LSPR effect (about the electric fields and hot electrons) and charge-carrier dynamics. Photoinduced charge separation near the resonant frequency is facilitated by the exponential enhancement of electromagnetic fields near the surface of plasmonic nanostructures under LSPR excitation. As a result of photoexcitation, a large number of high-energy carriers are generated, leading to the formation of electron-hole pairs on the surface of plasmonic catalysts, which can then be used to drive photocatalytic reactions [37]. It was determined by surface-enhanced Raman scattering (SERS) spectroscopy whether plasmonic nanocomposites exhibit enhanced localized electric fields. As shown in Fig. 4a, SERS spectra of methylene blue (MB) which is 10^{-5} M, serving as the probe molecule, absorbed on the photocatalysts are shown. Compared to bare TiO_2, the SERS signal intensities of MB on the series of L-TiNO plasmonic composites are significantly higher. The SERS signal intensity of MB on TiN substrate exhibits the largest enhancement, with a slight decrease with increasing oxide layer thickness. L-TiNO plasmonic composites exhibit strong LSPR and enhanced localized electric fields as a result of these observations. LSPR induces a significant electromagnetic field enhancement, increasing the formation rate and separation efficiency of photoexcited charge carriers, while decreasing the recombination rate. Consequently, compared to pure semiconductor materials, the L-TiNO plasmonic composites produces a greater number of energetic active carriers, which in turn enhance the photocatalytic CO_2 reduction activity.

To further confirm the enhanced carrier concentration resulting from the electric fields of the LSPR effect, Mott-Schottky curves were employed. In Fig. 4b, the Mott-Schottky curves for L-TiNO (with a slope, s = 0.72) and TiO_2 (with a slope, s = 1.57) are shown. The lower slope value for L-TiNO compared to TiO_2 indicates a higher carrier concentration on L-TiON. This observation supports the notion that the localized electric field enhancement induced by plasmon resonance coupling effect of L-TiNO leads to an increased concentration of photogenerated carriers, which ensures that more efficient carriers participate in the activation of CO_2.

As we mentioned former, the short lifetimes of hot carriers in LSPR materials limit their efficiency and application potential, so it is crucial to facilitate the fast transfer and separation of the enhanced photoinduced electron-hole pairs, which is promoted by the improved localized electromagnetic field, in order to promote the catalytic process. DFT calculations were conducted to elucidate the electronic structure and electron-hole transport mechanism on simulated TiO_2 (110), TiN (111) and L-TiNO composite. The models are shown in Figure S15. In particularly, we built the L-TiNO heterostructure model through coating 2 layers of TiO_2 (110) on TiN (111) to simulate the thin oxidation thickness of TiN. As shown in Figure S16, the total density of states (TDOS) reveal the increased charge density for L-TiNO compared to TiO_2 and TiN, which is the result of the enhanced light absorption and higher concentration of charge carriers in L-TiNO. To provide a more detailed analysis, local density of states (LDOS) and projected density of states (PDOS) were performed (Fig. 4c, S16 and S17). It can be found the charge redistribution after forming composites, especially, the energy levels from the coupling of Ti 3d orbitals and N 2p orbitals, which is the source of LSPR and metallic property produced by semiconductors, distributes in the band gap of TiO_2. And this coupling results in the formation of energy states within the band gap of TiO_2, which increases the adsorption of light and enhances the charge carrier concentration in L-TiNO. The interfacial electron transfer of L-TiNO was studied by calculating the work functions (Φ) of TiN and TiO_2, obtained by the energy difference between the vacuum and the Fermi energy level. As depicted in Figs. 4d and 4e, the Φ of TiN is lower (3.727 eV) compared to that of TiO_2 (4.4 eV). This difference in Φ values indicates that TiN has a lower energy barrier for electron transfer, indicating that TiN will donate electrons to TiO_2 when they are in contact, being in good agreement with the XPS results in Fig. 2. At the same time, the difference of Φ values also means that the difference of Fermi energy levels, giving rise to an energy barrier known as the Schottky barrier between TiN and

TiO_2, which can promote the transfer of charge carriers between interfaces. The differential charge density (DCD) was applied to further analyze the charge redistribution and the interfacial charge carrier transfer direction at the TiO_2-TiN interface in the L-TiNO composite, showing that electrons neighboring TiO_2 could be localized which means electrons transfer from TiN to TiO_2 again. (Fig. 4f). More intuitively, the visualization of the DCD (Δρ) through contour plots, Fig. 4g illustrates that the planar-averaged charge density difference along the Z-direction for L-TiNO is redistributed, As a result, electron accumulation occurs on the TiO_2 side (yellow region, positive DCD values) and electron depletion occurs on the TiN side (blue region, negative DCD values). Through this charge redistribution, an internal electric field is established between TiN and TiO_2 within the L-TiNO composite, which speeds up the spatial separation of carriers during photocatalysis.

Experimental techniques about charge separation and recombination dynamics were conducted to further investigate the behavior of electron-hole pairs. The steady-state fluorescence photoluminescence (PL) emission spectroscopy are depicted in Figure S18, showing that series of L-TiNO samples exhibit lower PL emission intensity compared to TiO_2 and TiN. This evidence is indicative of suppressed carrier recombination because of the built-in electric field in the L-TiNO composite after forming TiO_2-TiN interface. In comparison of different oxidation degrees, L-TiNO-500 exhibits the lowest PL emission intensity, suggesting the poorest recombination of electron-hole pairs. In contrast, for more highly oxidized samples, relatively strong electron and hole complexes were found. This finding may be attributed to the thick oxidation, which could result in the loss of charge transfer from TiN to TiO_2, thereby leaving the charge carrier behavior of TiO_2 predominantly. The optimal thickness of the TiO_2 layer for efficient charge generation and separation is about 13 nm, which is observed from TEM images. To further verify the capture of carriers, time-resolved photoluminescence (TRPL) spectroscopy were performed. As depicted in Fig. 4h, the longer average lifetime of carriers observed in L-TiNO (17.77248 ns) compared to pure TiN (11.33645 ns) and TiO_2 (11.42787 ns) is indicative of enhanced carrier capture and decreased carrier recombination. The extended carrier lifetime enhances carrier capture and transfer, while reducing carrier recombination Moreover, the formation of an internal electric field, resulting from the combination of LSPR TiN and semiconductor TiO_2, can increase the rate of photogenerated charge transport and effectively promote the separation of electrons and holes. Electrochemical impedance spectroscopy (EIS) Nyquist plots reveal smaller semicircle radius for charge-transfer resistance in the oxidation samples of L-TiNO series, indicating the fast carrier transfer because of the internal electric field and Schottky barrier which effectively promote charge transport (Figure S19). Also, L-TiNO-500 shows the smallest impedance. The photocurrent response curves exhibit series of L-TiNO samples has stronger transient photocurrent intensity than that of TiO_2 (0.146 μA cm^{-2}), of which L-TiNO-500 has the strongest one (0.68 μA cm^{-2}), proving the effective separation of photoexcited carriers (Fig. 4i). These observations indicate that the internal electric field built, along with the Schottky barrier, between the plasmonic TiN and TiO_2 semiconductor, improves the efficiency of carrier separation and migration, so that facilitates the interaction of carriers with reactants to participate in the desired chemical transformations and realizes the improved efficiency in photocatalytic properties on L-TiNO. Meanwhile, the thickness of the TiO_2 oxidation layer should be thin in order to efficiently utilize the hot electrons and shorten the migration distance to the surface active sites from the inner plasmonic TiN, because the average free range of electrons in TiN is only about 15 nm [38].

The strong internal electric field and LSPR effect between TiN and TiO_2 in the L-TiNO composite was verified by testing the surface potential via Kelvin probe force microscopy (KPFM) in Fig. 5, to deeply investigate separation behavior and spatial distribution of photogenerated charges under both dark and illumination conditions. The atomic force microscopy (AFM) images show the aggregation
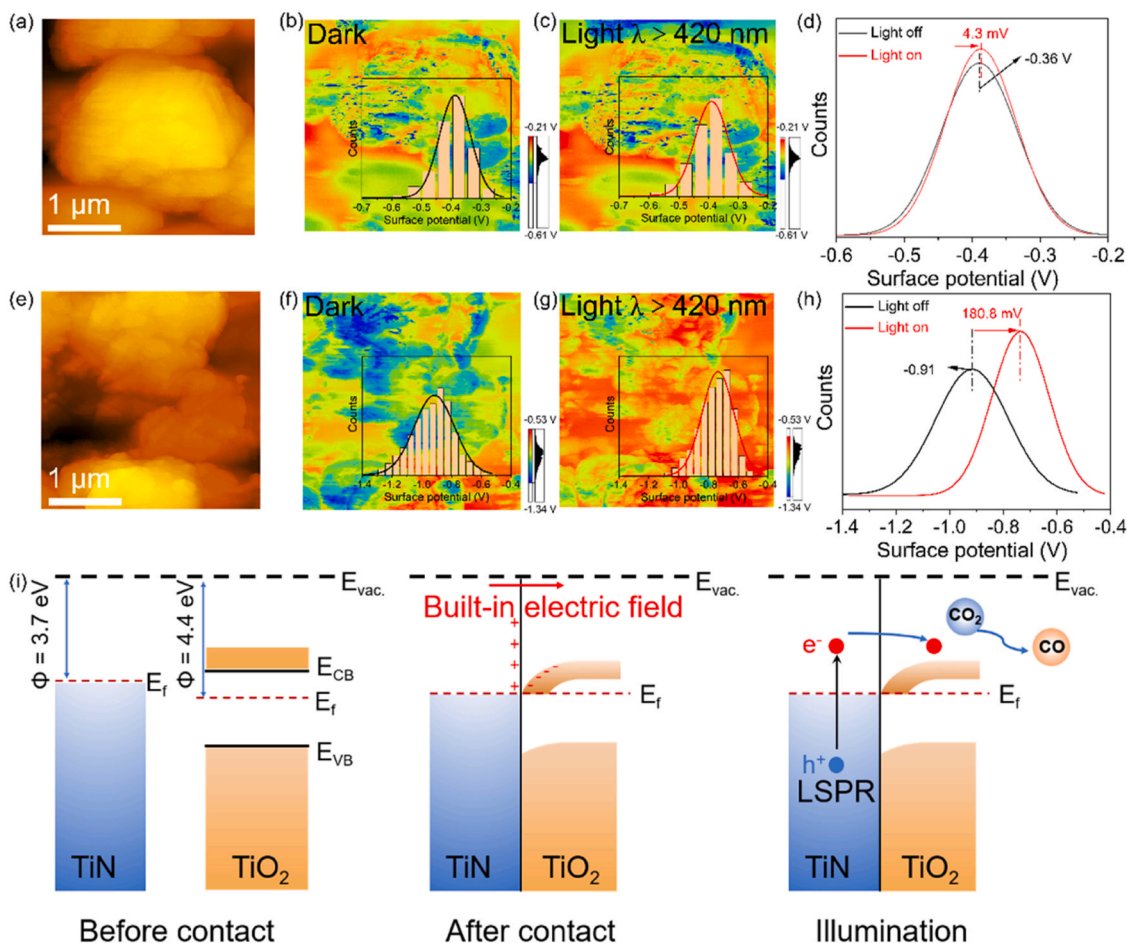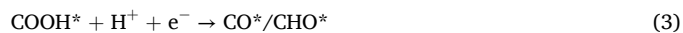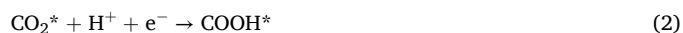
Fig. 5. AFM images of (a) TiO_2 and (e) L-TiNO. KPFM potential images of (b) TiO_2 (dark), (c) TiO_2 (light), (f) L-TiNO (dark) and (g) L-TiNO (light). Surface potential curves of (d) TiO_2 and (h) L-TiNO. (i) Schematic diagram of the band configuration and charge transfer at L-TiNO for visible-light driven CO_2 reduction.

nanoparticle morphology of TiO_2 (Fig. 5a) and L-TiNO (Fig. 5e), which are consistent with the results of SEM. Without irradiation, L-TiNO exhibits a significant higher intrinsic surface potential difference (−0.91 V) compared to TiO_2 (−0.36 V), confirming that the presence of a strong built-in electric field along Schottky barrier, which arises from the charge separation and redistribution at TiO_2-TiN interface (Figs. 5b, 5f and 5f, 5h). Comparing Figs. 5b-5c and Figs. 5f-5g, it can be seen noticeable surface potential differences before and after illumination on both TiO_2 and L-TiNO. More intuitively, before illumination, the surface potential of L-TiNO is more positiveat around −0.91 V compared to TiO_2 (-0.36 V), indicating that more hot electrons are injured to TiO_2 from TiN (Figs. 5d and 5h). Then, the surface potential of TiO_2 only increases by 4.3 mV (Fig. 5d) under illumination compared to the dark condition, while L-TiNO shows a substantial increase up to 180.8 mV (Fig. 5h). These results directly demonstrate that plasmon-semiconductor composite L-TiNO accumulates a large number of photogenerated holes on the surface when exposed to light. This accumulation of photogenerated holes is attributed to the LSPR effect, which enhances the localized electromagnetic field, thereby accelerating the generation of high-energy photoexcited carriers. Simultaneously, the verified formation of a built-in electric field, resulting from the difference in surface work function between TiO_2 and TiN, provides strong evidence for acting as a driving force to facilitate the efficient migration and separation of photogenerated electrons and holes (Fig. 5i).

3.4. Mechanism on CO_2 reduction process

To infer the CO_2 reduction routing occurring on L-TiNO and

understand the role of the metal oxide-substrate-structured TiO_2-TiN composite with built-in-electric field, *in situ* FTIR spectroscopy was employed to monitor the intermediates produced during the photocatalytic CO_2 reduction reaction. The respective attributions and references of the bands are listed in Table S3. As shown in Fig. 6a, the peak at 1208 cm^{-1} is deduced to correspond to the asymmetric stretching of the HCO_3* group [39]. The peaks observed near 1643 cm^{-1} are attributed to COOH* groups, which are crucial intermediates in the conversion of CO_2 to CO or CH_4 [40]. The peaks associated with CH_3O*at 1016 and 1157 cm^{-1}, CH_2O* at 1507 cm^{-1} and CHO* at 1464 cm^{-1}, which are indicative of CH_4 production, are found to be insignificant [39,41]. Of particular importance are the peaks observed at 1739 and 2100 cm^{-1}, which are associated with bridged and linearly bonded CO* intermediates absorbing on L-TiNO, respectively [42]. These CO* intermediates plays a significant role in subsequent processes such as CO (g) desorption, hydrogenation or C-C coupling. It is noteworthy that the intensities of all these intermediates peaks gradually increase with increasing irradiation time, indicating the continuous progress of the photocatalytic reaction. Based on the *in situ* FTIR analysis, the most probable photocatalytic CO_2 reduction reaction pathways on L-TiNO are explained as follows:

$$CO_2 + * \rightarrow CO_2* \tag{1}$$

$$CO_2* + H^+ + e^- \rightarrow COOH* \tag{2}$$

$$COOH* + H^+ + e^- \rightarrow CO*/CHO* \tag{3}$$

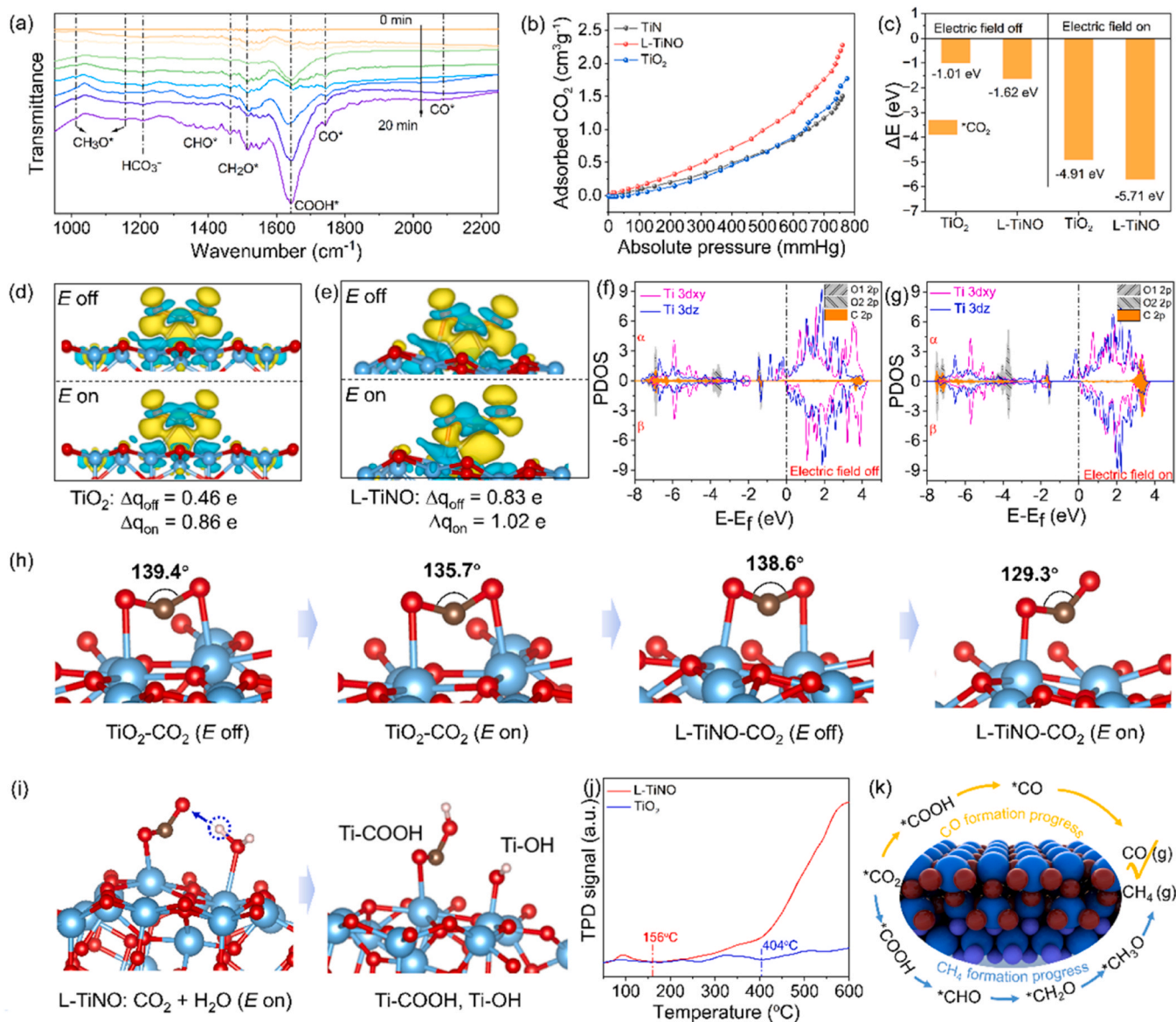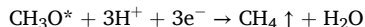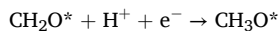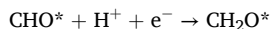$$CO* \rightarrow CO \uparrow \tag{4}$$

Fig. 6. (a) *In situ* FTIR spectra for reaction intermediates on L-TiNO at different irradiation times. (b) CO_2 adsorption curves of TiN, L-TiNO and TiO_2. (c) Calculated CO_2 adsorption energy of the simulated TiO_2 and L-TiNO with electric on/off. (d, e) Charge density differences after CO_2 adsorption of the simulated TiO_2 and L-TiNO with electric on/off. PDOS of CO_2 adsorbed on L-TiNO in the absence (f) and presence (g) of electric field. (h) Shape of CO_2 adsorption in various conditions. (i) Model of H_2O molecule absorbed on L-TiNO with electric field. (j) CO-TPD curves of TiO_2 and L-TiNO. (k) Scheme of CO_2 conversion pathway on L-TiNO.

$$CHO^* + H^+ + e^- \rightarrow CH_2O^* \tag{5}$$

$$CH_2O^* + H^+ + e^- \rightarrow CH_3O^* \tag{6}$$

$$CH_3O^* + 3H^+ + 3e^- \rightarrow CH_4 \uparrow + H_2O \tag{7}$$

where the "*" denotes active sites, and the "↑" represents the release of the gas product.

According to the reaction pathways, CO_2 adsorption and CO^* desorption are key factors for activity and selectivity, respectively, in CO_2 reduction reaction. A detailed analysis of the CO_2 activation process was conducted. From CO_2 adsorption isotherms in Fig. 6b, L-TiNO has a higher CO_2 adsorption capacity of 2.26 cm^3 g^{-1} under 1 atm at 25 °C, which is about 1.28 times larger than that of pure TiO_2 (1.76 cm^3 g^{-1}), indicating that the formation of TiO_2-TiN composite favors CO_2 adsorption, which is the prerequisite step for triggering subsequent CO_2 reduction, making it a determining factor for the activity of the photocatalyst in degree. The adsorption and activation of CO_2 on the photocatalysts were also investigated via DFT calculations. As shown in Fig. 6c, the CO_2 adsorption energy on L-TiNO (−1.62 eV) is more

negative compared to TiO_2 (−1.01 eV), implying the stronger adsorption of CO_2 on L-TiNO. Additionally, the Bader charge and DCD results from the calculations reveal that more electrons transfer from L-TiNO to CO_2 (0.83 e^-) than from TiO_2 (0.46 e^-), further indicating the enhanced CO_2 activation on L-TiNO (Figs. 6d and 6e). We also calculated the CO_2 adsorption by adding an electric field to simulate the locally enhanced electric field generated by the LSPR effect. As shown in Figs. 6c-6e and **S20**, when the electric field is present, L-TiNO shows the most negative CO_2 adsorption energy of −5.71 eV and the largest transfer number of electrons to CO_2 (1.02 e^-). These results manifest that TiO_2-TiN composite with localized strong electric field enhances the stability of the key absorbed configuration, promoting CO_2 adsorption by the surface oxide layer and driving the reaction. Moreover, the atomic-level behaviors of CO_2 adsorption on the samples were analyzed using density of states (DOS) calculations with CO_2 adsorption on the models. The calculated DOS and PDOS results, as show in the provided Figs. 6f and 6g, indicate that the state peaks of O_1 2p and O_2 2p orbitals of the absorbed CO_2 molecule shift towards lower energy and form a larger

overlap area with more localized Ti 3dz (parallel to the electric field) states when an electric field is introduced to the hybrid states compared to when the electric field is turned off. These results manifest that the localized strong electric field introduced by plasma resonance enhances the interaction between CO_2 and L-TiNO, promoting the adsorption and activation of CO_2.

Additionally, the CO_2 adsorption models shown in the provided Fig. 6**h** also reveal structural changes in the absorbed CO_2 molecule when the electric field is turned off and on. Specifically, it can be observed that the angle of the absorbed CO_2 molecule changes from 138.62° (electric field is off) to 129.28° (electric field is on). This change makes it possible to create more space for the adjacent Ti sites to absorb water (H_2O) molecules and undergo dissociate H_2O to release H* species for reducing CO_2* to COOH*(Fig. 6**i**). In this case, the surface of the catalyst after reaction is supposed to have terminal hydroxyl groups (Ti−OH). FTIR measurements conducted before and after CO_2 reduction were performed in Figure S21. The broad band at 3300–3500 cm^{-1} in L-TiNO FTIR after CO_2 reduction reaction shows the O-H stretching vibrations of Ti-OH [43]. This confirms that the formation of L-TiNO composite with SOSI promotes the provision of protons during the reaction and fabricate Ti−OH surface statea after the reaction. Meanwhile, CO* tends to desorb as CO(g) rather than undergoing further hydrogenation to CHO*. This behavior can be attributed to the formation of SOSI that the reducing oxide TiO_2 provides hydrogen spillover channel, allowing the hydrogen component to be transported to the substrate TiN, and impeding the hydrogenation of CO* so that facilitating its desorption. According to Fig. 6**h**, the O atom in the CO_2 molecule forms a bond with the Ti atom on the TiO_2 surface, enabling the adsorption of CO_2 on the TiO_2 surface. The excited electron is transferred from the conduction band to the C atom of CO_2, and through the intermediate COOH*, it is reduced to CO*. Finally, the CO molecule dissociates, resulting in the reduction of CO_2 to CO(g). CO temperature programmed desorption (TPD) curves were provided to explore the desorption abilities of CO on the samples. As shown in Fig. 6**j**, L-TiNO shows the lowest onset desorption temperature (156 ℃) for CO desorption, further confirming that CO(g) is easily released from the surface of L-TiNO. This behavior suggest that L-TiNO possesses a higher selectivity for the conversion of CO_2 to CO. Based on the aforementioned results and findings, the photocatalytic CO_2 reduction reaction occurring on L-TiNO can be depicted in Fig. 6**k**. The conversion route of "CO_2 → COOH* → CO" is illustrated, highlighting the crucial role of strong electronic effects. More specifically, the alternative electric field and hot carriers generated by the LSPR effect from TiN would promote efficient carrier transfer and accumulation of electrons on the surface of active sites, thereby enhancing both light and CO_2 adsorption. Furthermore, the formation of SOSI between TiO_2 and TiN facilities the dissociation of H_2O molecule and provides hydrogen spillover channel to improve CO selectivity. These findings contributed to more in-depth understanding of the design and optimization of TiN-based catalysts for efficient photocatalytic CO_2 reduction.

4. Conclusion

In summary, the modification of plasmonic TiN nanoparticles with surface oxidation to create the L-TiNO composite has led to the successful development of a semiconductor-coated plasmonic material. The obtained L-TiNO exhibits excellent CO_2-to-CO conversion activity, with a high generation rate of 50.8 μmol g^{-1} h^{-1} and a selectivity of 95.98% in pure water under visible light irradiation. The formation of the composite extends the light adsorption edge to the visible region, significantly enhancing the utilization of solar energy. It also greatly prolongs the lifetimes of carriers, allowing for more efficient charge separation and migration, which in turn promotes the CO_2 reduction activity. KPFM and DFT calculation results provides strong evidence for the presence of the built-in electric field from TiN to TiO_2 and the generation of hot carriers, which contribute to the efficient separation

and migration of the carriers. Meanwhile, *in situ* FTIR analysis clearly illustrates the conversion route of CO_2 to CO through the formation of COOH* intermediates. We find that: the effect of SOSI promotes the accumulation of electrons to get strong CO_2 adsorption ability, the electric field modifies the shape of the absorbed CO_2 and facilitates the dissociation of H_2O to provide protons for COOH* formation, and TiO_2 thin oxidation layer provides hydrogen spillover channel to drive the desorption of CO* to CO(g). Overall, our study highlights the potential of utilizing isoexciton-induced catalysis for efficient and sustainable CO_2 reduction and opens up new possibilities for the creation of low-cost and efficient photocatalysts with practical applications in CO_2 reduction.

CRediT authorship contribution statement

Yulin Min: Writing – review & editing, Supervision, Resources, Project administration, Funding acquisition, Conceptualization. **Shuaiqi Gong:** Writing – review & editing, Visualization, Validation, Supervision, Software, Resources, Project administration, Conceptualization. **Sheng Xu:** Software, Formal analysis, Data curation. **Huiming Wang:** Writing – original draft, Visualization, Validation, Resources, Formal analysis, Data curation. **Gregory A Solan:** Writing – review & editing, Software, Project administration, Formal analysis. **Jinting Xu:** Writing – review & editing, Resources, Project administration, Conceptualization. **Baoxin Ni:** Validation, Formal analysis, Conceptualization.

Declaration of Competing Interest

The authors declare that they have no known competing financial interests or personal relationships that could have appeared to influence the work reported in this paper.

Data Availability

Data will be made available on request.

Notes

The authors have no conflict of interest to declare.

Appendix A. Supporting information

Supplementary data associated with this article can be found in the online version at doi:10.1016/j.apcatb.2024.124141.

References

[1] K. Maeda, Metal-Complex/Semiconductor Hybrid Photocatalysts and Photoelectrodes for CO_2 Reduction Driven by Visible Light, Adv. Mater. 31 (25) (2019) 1808205.

[2] B. Ni, G. Zhang, H. Wang, Y. Min, K. Jiang, H. Li, Correlating oxidation state and surface ligand motifs with the selectivity of CO_2 photoreduction to C_2 products, Angew. Chem. 135 (6) (2023) e202215574.

[3] M. Yang, P. Wang, Y. Li, S. Tang, X. Lin, H. Zhang, Z. Zhu, F. Chen, Graphene aerogel-based NiAl-LDH/g-C_3N_4 with ultratight sheet-sheet heterojunction for excellent visible-light photocatalytic activity of CO_2 reduction, Appl. Catal. B: Environ. 306 (2022) 121065.

[4] S. Gong, Y. Niu, X. Liu, C. Xu, C. Chen, T.J. Meyer, Z. Chen, Selective CO_2 photoreduction to acetate at asymmetric ternary bridging sites, ACS Nano 17 (5) (2023) 4922–4932.

[5] L. Liu, S. Wang, H. Huang, Y. Zhang, T. Ma, Surface sites engineering on semiconductors to boost photocatalytic CO_2 reduction, Nano Energy 75 (2020) 104959.

[6] B. Ni, H. Jiang, W. Guo, Q. Xu, Y. Min, Tailoring the oxidation state of metallic TiO through Ti^{3+}/Ti^{2+} regulation for photocatalytic conversion of CO_2 to C_2H_6, Appl. Catal. B: Environ. 307 (2022) 121141.

[7] E. Gong, S. Ali, C.B. Hiragond, H.S. Kim, N.S. Powar, D. Kim, H. Kim, S.-I. In, Solar fuels: research and development strategies to accelerate photocatalytic CO_2 conversion into hydrocarbon fuels, Energy Environ. Sci. 15 (3) (2022) 880–937.

[8] C. Hu, X. Chen, J. Low, Y.-W. Yang, H. Li, D. Wu, S. Chen, J. Jin, H. Li, H. Ju, C.-H. Wang, Z. Lu, R. Long, L. Song, Y. Xiong, Near-infrared-featured broadband CO_2 reduction with water to hydrocarbons by surface plasmon, Nat. Commun. 14 (1) (2023) 221.

[9] G.V. Naik, V.M. Shalaev, A. Boltasseva, Alternative plasmonic materials: beyond gold and silver, Adv. Mater. 25 (24) (2013) 3264–3294.

[10] W. Tu, Y. Zhou, Z. Zou, Photocatalytic conversion of CO_2 into renewable hydrocarbon fuels: state-of-the-art accomplishment, challenges, and prospects, Adv. Mater. 26 (27) (2014) 4607–4626.

[11] S.C. Warren, E. Thimsen, Plasmonic solar water splitting, Energy Environ. Sci. 5 (1) (2012) 5133–5146.

[12] Q. Zhang, Z. Zuo, D. Ma, Plasmonic nanomaterials for solar-driven photocatalysis, Chem. Commun. 59 (50) (2023) 7704–7716.

[13] R. Li, X. Wang, M. Chen, Non-NOble Metal and Nonmetallic Plasmonic Nanomaterials with Located Surface Plasmon Resonance Effects: Photocatalytic Performance and Applications, Catalysts 13 (6) (2023) 940.

[14] H. Chen, L. Shao, Q. Li, J. Wang, Gold nanorods and their plasmonic properties, Chem. Soc. Rev. 42 (7) (2013) 2679–2724.

[15] S. Linic, P. Christopher, D.B. Ingram, Plasmonic-metal nanostructures for efficient conversion of solar to chemical energy, Nat. Mater. 10 (12) (2011) 911–921.

[16] J. Yang, L. Li, C. Xiao, Y. Xie, Dual-Plasmon Resonance Coupling Promoting Directional Photosynthesis of Nitrate from Air. Angew. Chem. 62 (47) (2023) e202311911.

[17] X. Liu, Z. Fang, X. Teng, Y. Niu, S. Gong, W. Chen, T.J. Meyer, Z. Chen, Paired formate and H_2 productions via efficient bifunctional Ni-Mo nitride nanowire electrocatalysts, J. Energy Chem. 72 (2022) 432–441.

[18] R. Xue, P. Ge, J. Xie, Z. Hu, X. Wang, P. Li, Controllable CO_2 reduction or hydrocarbon oxidation driven by entire solar via silver quantum dots direct photocatalysis, Small 19 (20) (2023) 2207234.

[19] Y. Jiang, S. Li, S. Wang, Y. Zhang, C. Long, J. Xie, X. Fan, W. Zhao, P. Xu, Y. Fan, C. Cui, Z. Tang, Enabling specific photocatalytic methane oxidation by controlling free radical type, J. Am. Chem. Soc. 145 (4) (2023) 2698–2707.

[20] S. Bai, W. Jing, G. He, C. Liao, F. Wang, Y. Liu, L. Guo, Near-infrared-responsive photocatalytic CO_2 conversion via in situ generated Co_3O_4 /Cu_2O, ACS Nano 17 (11) (2023) 10976–10986.

[21] S. Ishii, S.L. Shinde, W. Jevasuwan, N. Fukata, T. Nagao, Hot electron excitation from titanium nitride using visible light, ACS Photonics 3 (9) (2016) 1552–1557.

[22] M.B. Cortie, J. Giddings, A. Dowd, Optical properties and plasmon resonances of titanium nitride nanostructures, Nanotechnology 21 (11) (2010) 115201.

[23] X. Xu, A. Dutta, J. Khurgin, A. Wei, V.M. Shalaev, A. Boltasseva, TiN@TiO_2 Core–Shell nanoparticles as plasmon-enhanced photosensitizers: the role of hot electron injection. Laser Photonics Rev. 14 (5) (2020) 1900376.

[24] M.L. Brongersma, N.J. Halas, P. Nordlander, Plasmon-induced hot carrier science and technology, Nat. Nanotechnol. 10 (1) (2015) 25–34.

[25] J. Zhang, T.P. Chen, X.D. Li, Y.C. Liu, Y. Liu, H.Y. Yang, Investigation of localized surface plasmon resonance of TiN nanoparticles in TiN_xO_y thin films, Opt. Mater. Express 6 (7) (2016) 2422.

[26] P. Patsalas, N. Kalfagiannis, S. Kassavetis, Optical properties and plasmonic performance of titanium nitride, Materials 8 (6) (2015) 3128–3154.

[27] C. Zhan, X.-J. Chen, J. Yi, J.-F. Li, D.-Y. Wu, Z.-Q. Tian, From plasmon-enhanced molecular spectroscopy to plasmon-mediated chemical reactions, Nat. Rev. Chem. 2 (9) (2018) 216–230.

[28] W. He, J. Xiong, Z. Tang, Y. Wang, X. Wang, H. Xu, Z. Zhao, J. Liu, Y. Wei, Localized surface plasmon resonance effect of bismuth nanoparticles in Bi/TiO_2 catalysts for boosting visible light-driven CO_2 reduction to CH_4, Appl. Catal. B: Environ. (2023) 123651.

[29] M. Tan, Y. Yang, Y. Yang, J. Chen, Z. Zhang, G. Fu, J. Lin, S. Wan, S. Wang, Y. Wang, Hydrogen spillover assisted by oxygenate molecules over nonreducible oxides, Nat. Commun. 13 (1) (2022) 1457.

[30] S. Zou, L. Wang, H. Wang, X. Zhang, H. Sun, X. Liao, J. Huang, A.R. Masri, Structure-performance correlation on bimetallic catalysts for selective CO_2 hydrogenation, Energy Environ. Sci. 16 (11) (2023) 5513–5524.

[31] A. Mahdavi-Shakib, T.N. Whittaker, T.Y. Yun, K.B. Sravan Kumar, L.C. Rich, S. Wang, R.M. Rioux, L.C. Grabow, B.D. Chandler, The role of surface hydroxyls in the entropy-driven adsorption and spillover of H_2 on Au/TiO_2 catalysts, Nat. Catal. 6 (8) (2023) 710–719.

[32] H. Kang, L. Zhu, S. Li, S. Yu, Y. Niu, B. Zhang, W. Chu, X. Liu, S. Perathoner, G. Centi, Y. Liu, Generation of oxide surface patches promoting H-spillover in Ru/(TiO_x)MnO catalysts enables CO_2 reduction to CO, Nat. Catal. (2023) 1–11.

[33] X. Wang, X. Zhong, L. Bai, J. Xu, F. Gong, Z. Dong, Z. Yang, Z. Zeng, Z. Liu, L. Cheng, Ultrafine titanium monoxide (TiO_{1+x}) nanorods for enhanced sonodynamic therapy, J. Am. Chem. Soc. 142 (14) (2020) 6527–6537.

[34] C. Foo, Y. Li, K. Lebedev, T. Chen, S. Day, C. Tang, S.C.E. Tsang, Characterisation of oxygen defects and nitrogen impurities in TiO_2 photocatalysts using variable-temperature X-ray powder diffraction, Nat. Commun. 12 (1) (2021) 661.

[35] A. Beniya, S. Higashi, Towards dense single-atom catalysts for future automotive applications, Nat. Catal. 2 (7) (2019) 590–602.

[36] S. Pétigny, H. Mostéfa-Sba, B. Domenichini, E. Lesniewska, A. Steinbrunn, S. Bourgeois, Superficial Defects Induced by Argon and Oxygen Bombardments on (110) TiO_2 Surfaces, Surf. Sci. 410 (2–3) (1998) 250–257.

[37] Y. Li, Y. Lei, D. Li, A. Liu, Z. Zheng, H. Liu, J. Guo, S. Liu, C. Hao, D. He, Recent progress on photocatalytic CO_2 conversion reactions over plasmonic metal-based catalysts, ACS Catal. 13 (15) (2023) 10177–10204.

[38] J.S. Chawla, X.Y. Zhang, D. Gall, Effective electron mean free path in TiN(001), J. Appl. Phys. 113 (6) (2013) 063704.

[39] X. Li, L. Li, G. Chen, X. Chu, X. Liu, C. Naisa, D. Pohl, M. Löffler, X. Feng, Accessing parity-forbidden d-d transitions for photocatalytic CO_2 reduction driven by infrared light, Nat. Commun. 14 (1) (2023) 4034.

[40] J. Xu, Z. Ju, W. Zhang, Y. Pan, J. Zhu, J. Mao, X. Zheng, H. Fu, M. Yuan, H. Chen, R. Li, Efficient infrared-light-driven CO_2 reduction over ultrathin metallic Ni-doped CoS_2 Nanosheets. Angew. Chem. 60 (16) (2021) 8705–8709.

[41] L.C. Grabow, M. Mavrikakis, Mechanism of methanol synthesis on Cu through CO_2 and CO hydrogenation, ACS Catal. 1 (4) (2011) 365–384.

[42] G.E. Ewing, W.E. Thompson, G.C. Pimentel, Infrared detection of the formyl radical HCO, J. Chem. Phys. 32 (3) (1960) 927–932.

[43] Y. Gao, Y. Masuda, W.S. Seo, H. Ohta, K. Koumoto, TiO_2 nanoparticles prepared using an aqueous peroxotitanate solution, Ceram. Int. 30 (7) (2004) 1365–1368.